Imaging of oxide dielectrics by near-field microwave microscopy

Qinxin Zhang*, Paul J. McGinn

*Department of Chemical and Biomolecular Engineering, Center for Molecularly Engineered Materials,
University of Notre Dame, Notre Dame, IN 46556, USA*

Abstract

Scanning near-field microwave microscopy was used to image $LaAlO_3$ and TiO_2 single crystals and bulk yttria-stabilized zirconia (YSZ) polycrystalline ceramic microstructures. The effect of microstructural features including grain boundaries, twins, surface roughness, and oxygen content variations on the local dielectric constant, and the resulting microscope image quality are discussed.
© 2004 Elsevier Ltd. All rights reserved.

Keywords: Near-field microwave microscopy; Dielectric properties; Microstructure; $LaAlO_3$; TiO_2

1. Introduction

Advanced electroceramic materials with high permittivity, high quality factor, and good temperature stability are commercially important for use as dielectric resonators, filters, and other key components for microwave communications applications (about 0.5–20 GHz).[1] Typically, microwave properties measurements are performed on the length scale of the free space wavelength of the microwave signal, which is about 12.5 cm at 2.4 GHz. Measured properties, therefore, represent an average over the length of the sample. For a better understanding of the microstructural dependence of the materials microwave response, it is desirable to be able to characterize dielectric materials on the length scale of extrinsic defects, which are responsible for most of the non-linear behavior. An improved understanding of the impact of defects (including strain, composition variations, interphase boundaries, and grain boundaries) on the local dielectric properties of electroceramics at high frequencies can be used to aid in the design of improved microwave devices.

Many reports in the literature have attempted to correlate dielectric properties with characteristics such as grain size, doping level, density, or crystal structure, but this has not been readily accomplished on a local scale. The relatively new technique of near-field scanning microwave microscopy (SMM) can permit characterization of the effects of inhomogeneities and defects in crystals, films, and compacts on the local dielectric behavior. SMM builds on recent developments in the field of scanning probe microscopy. Several recent reviews trace the history of this development.[2,3] In particular, SMM is closely related to near-field scanning optical microscopy (NSOM). In effect, by replacing the optical fiber used in NSOM with a microwave cavity, the local response of a sample to microwave excitation can be characterized. Changes in the cavity's resonant frequency and quality factor will depend on the properties of a sample positioned near the tip which extends from the cavity. By moving the tip/cavity assembly over a surface, one can map the cavity resonant frequency f_r and quality factor Q as a function of position and generate images of the sample. In addition to qualitative images, the microscope can provide quantitative characterization of local dielectric properties.

Several studies have shown the usefulness and versatility of these instruments for dielectric characterization. Steinhauer et al.[4] used a SMM to image the permittivity and tunability of $BaSrTiO_3$ films. Wang et al.[5] studied local dielectric constant and loss tangent in periodic domains in $PbTiO_3$ films. Chang et al.[6] used a SMM to identify low-loss compositions in combinatorial discovery studies of thin film libraries. However, only a limited number of investigations have concerned bulk polycrystalline or single crystal ceramics.[7]

The purpose of the present study is to apply the SMM to examination of simple microstructural features in bulk

* Corresponding author.
E-mail address: qzhang@nd.edu (Q. Zhang).

dielectric materials. The intention is to be able to distinguish the SMM image contrast effects of microstructural features from those caused by the artifacts resulting from sample preparation or from instrumentation effects.

2. Experimental procedures

The core component of the SMM is a resonator/tip assembly. The microscope used for dielectric characterization in this study is manufactured by Ariel Technologies (Model EMP2000), and employs a tip/cavity design shown schematically in Fig. 1. The probe employs a high-Q $\lambda/4$ coaxial resonator with a sapphire dielectric. There is a small aperture at the end of the cavity, through which extends a sharp metal tip (essentially a tungsten scanning tunneling microscope tip) that is mounted to the center of an invar conductor. An invar metal cavity cover and a silver coating on the aperture provide shielding. The aperture size, tip diameter, and extended length of the tungsten tip are much smaller than the microwave wavelength, so only evanescent microwaves are emitted from the tip. The interaction of propagating evanescent microwaves with a sample near the tip changes the resonant frequency of the resonator. Thus, the sample's dielectric constant can be described in terms of the change of the resonant frequency of the cavity.

The intrinsic spatial resolution of a scanning evanescent microwave microscope depends on the tip size and the sample's dielectric properties. The sharper the tip, the higher the imaging resolution will be. Two tips can be used in the EMP2000, with the "sharp" tip having a tip diameter about 10–20 μm, while the "spherical" tip has a diameter of approximately 150 μm. The spherical tip is used to provide more accurate quantitative measurement of the dielectric properties of the dielectric materials when the tip

contacts the sample. However, the sphere tip will reduce the spatial imaging resolution. The sphere tip is made by a dc discharging method, while the sharp tip is made by an electrochemical lamellae etching method.[8] The spatial resolution will also improve with an increase in the dielectric constant of the sample. Gao and Xiang[9] have shown that the relationship of resonant frequency shift and sample dielectric constant for the tip design shown in Fig. 1, for the case when the tip contacts the sample is as follows:

$$\frac{\Delta f_r}{f_r} = A \left(\ln \frac{1-b}{b} + 1 \right),$$

$$b = \frac{\varepsilon - \varepsilon_0}{\varepsilon + \varepsilon_0}.$$

Here, f_r is the resonant frequency of the cavity in the absence of a sample; Δf_r is the change in resonant frequency caused by the sample; and ε_0 is free space permittivity, while ε is the sample permittivity. The constant A is determined by the geometry of the resonator/tip assembly, and can be determined by measuring the resonant frequencies of samples (ideally, single crystals) with known dielectric constants. The calibration curve to determine A for a tip/resonator assembly employed in this study is shown in Fig. 2. The dielectric constant values for the single crystals were taken from the literature. After the calibration curve has been determined, the unknown dielectric constant of a sample can be determined by measuring the resonant frequency of the cavity. The calibration curve shows that a single crystal with higher dielectric constant has a lower resonant frequency.

An "approaching curve," shown in Fig. 3, is used to determine the point of tip-sample contact. The approaching curve is obtained by recording the resonant frequencies and
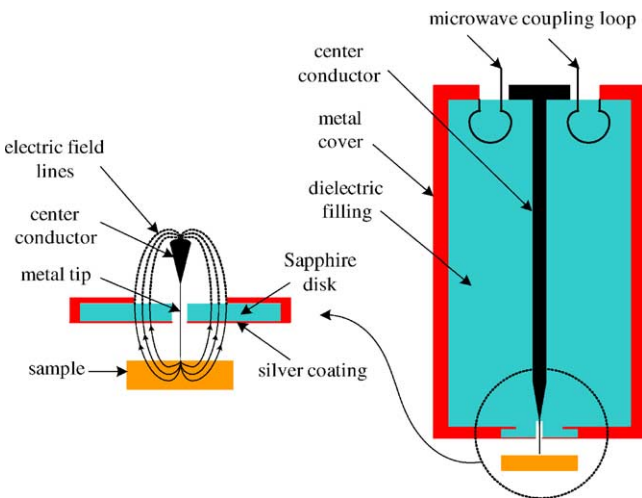

Fig. 1. Schematic diagram of the SMM resonator/tip assembly. The metal cover and silver coating shield the propagating waves, so that only evanescent microwaves are emitted from the tip.
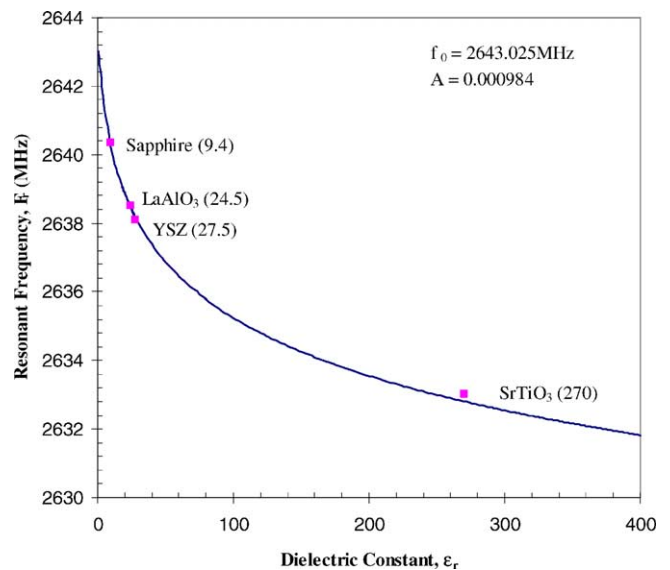

Fig. 2. Relationship of resonant frequency and sample dielectric constant for one of the resonator cavities used in this work. The value for each single crystal with known dielectric constant was measured at the contact point (Fig. 3).
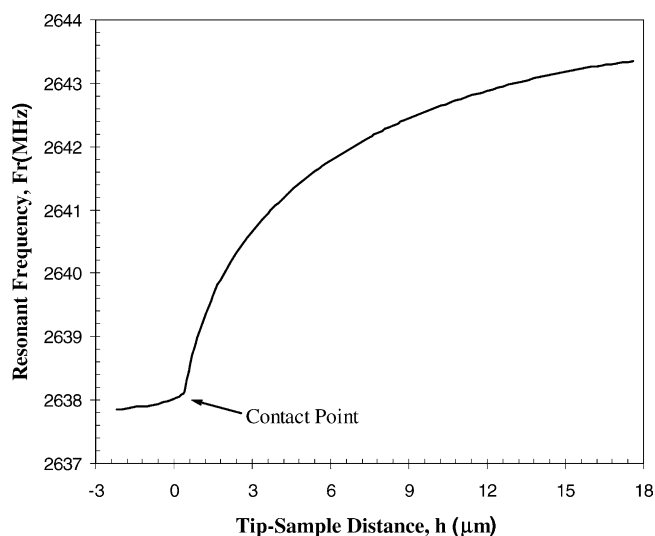
Fig. 3. SMM approaching curve on a LaAlO$_3$ single crystal showing the point of contact of the tip with the sample.

quality factors as the tip approaches the sample surface. As seen from the figure, the approaching curve shows that tip-sample distance affects the resonant frequency. As a result, sample topography is an important consideration in imaging dielectric surfaces, necessitating careful sample surface preparation. For example, Fig. 4 shows a SMM image of a poorly polished sapphire single crystal surface. The change in height due to scratches causes local changes in resonant frequency, representing apparent changes in the dielectric constant.

Several scanning modes can be used for imaging. In order to minimize topography effects, the tip can always contact the sample surface during scanning, in what is termed soft-contact mode. This mode is preferred for imaging microstructural features in dielectrics, as opposed to constant-height scanning mode, which is sensitive to topography effects. A third scanning mode, termed constant-frequency scanning, involves continuously vary-

ing the z height in order to maintain a constant resonant frequency. This offers the possibility for producing a topographic image of a dielectrically uniform material. However, in bulk ceramics, large variations in dielectric constant, such as results from scanning across a pore, can lead to catastrophic crashing of the tip into the sample surface. In the present study, bulk samples were carefully polished to minimize sample topography artifacts and relatively pore-free regions were examined. Finally, in the EMP2000, the cavity is attached to a piezoelectric tube, which provides precise small-scale (<50 μm) scan. Motors beneath the sample stage provide larger scale (50 μm–50 mm) scanning capability. Both types of images are presented here.

3. Results

The goal of this work was to examine several samples with representative effects that one would expect to encounter in typical polycrystalline dielectrics. Samples were chosen to isolate particular effects in the hopes of limiting the complexity of image interpretation.

3.1. Twin structures in LaAlO$_3$ substrates

Lanthanum aluminate (LAO) single crystals are often used as thin film substrates since they have a relatively low dielectric constant, a low-loss tangent and good chemical stability. At room temperature, LaAlO$_3$ has a perovskite structure with a slight rhombohedral distortion, while it exhibits a cubic symmetry above 500–600 °C. Thus, on cooling from elevated temperatures LaAlO$_3$ undergoes a structural phase transition from cubic to rhombohedral structure that is typically accompanied by twin formation. The formation of ⟨1 0 0⟩ and ⟨1 1 0⟩ twins releases the strain caused by the lattice distortion of the structural transition. The formation of ⟨1 0 0⟩ twins relieves more strain energy than ⟨1 1 0⟩, so they are more numerous.[10–13] The strain associated with
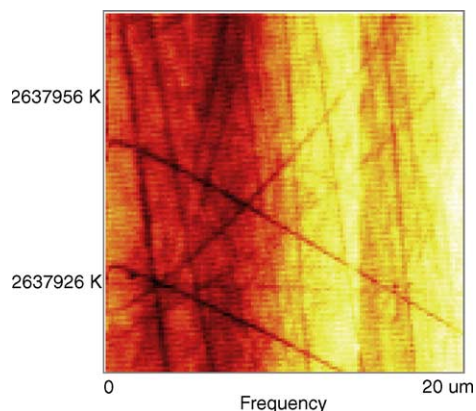

Fig. 4. Resonant frequency profile on a poorly polished sapphire single crystal, scanned in constant-height mode. The topography effects by scratches on the resonant frequency are seen.
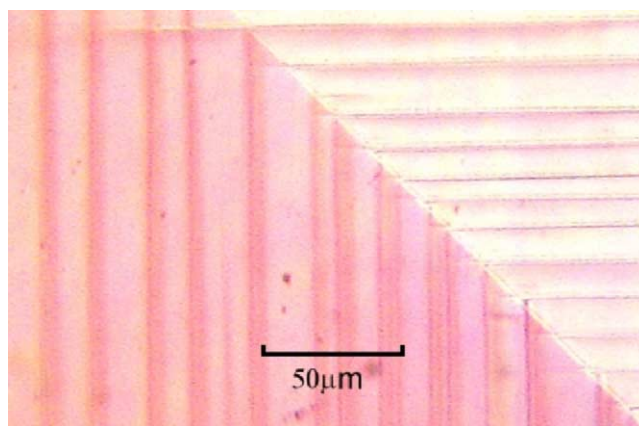
Fig. 5. Polarized optical microscope image of a LaAlO$_3$ crystal exhibiting both ⟨1 1 0⟩ and ⟨1 0 0⟩ twins.

twin structures will affect the local dielectric properties, thus, producing contrast in an SMM image. For example, Hyun et al.[7] studied the twin domains in LaAlO$_3$ with a scanning microwave microscope. They reported that changes in the dielectric constant were larger on $\langle 1\,1\,0 \rangle$ twin domains than on $\langle 1\,0\,0 \rangle$ domains.

In the present work, a commercially available LAO $(1\,0\,0)$ crystal (MTI crystal) was examined. Fig. 5 shows a polarized optical microscope image of the twin structures. AFM examination of the crystal showed that the surface was relatively smooth, with a roughness less than 50 nm. Although

twinning can result in the formation of surface relief, with step heights as large as 25 nm being reported by Sum et al.[14], gross topographic effects of the type discussed earlier can be neglected. Dielectric constant images of the LaAlO$_3$ crystal are shown in Fig. 6a and b, for two different scan ranges. In both of the images, the colors represent the local dielectric constant corresponding to the scale shown to the right of the figure. Fig. 6c shows lower magnification resonant frequency (left) and Q (right) images. The twin structures can be clearly observed in these SMM images. The region between the $\langle 1\,0\,0 \rangle$ twin pairs has a lower dielectric constant and lower Q than the native crystal. The $\langle 1\,1\,0 \rangle$ twins are the
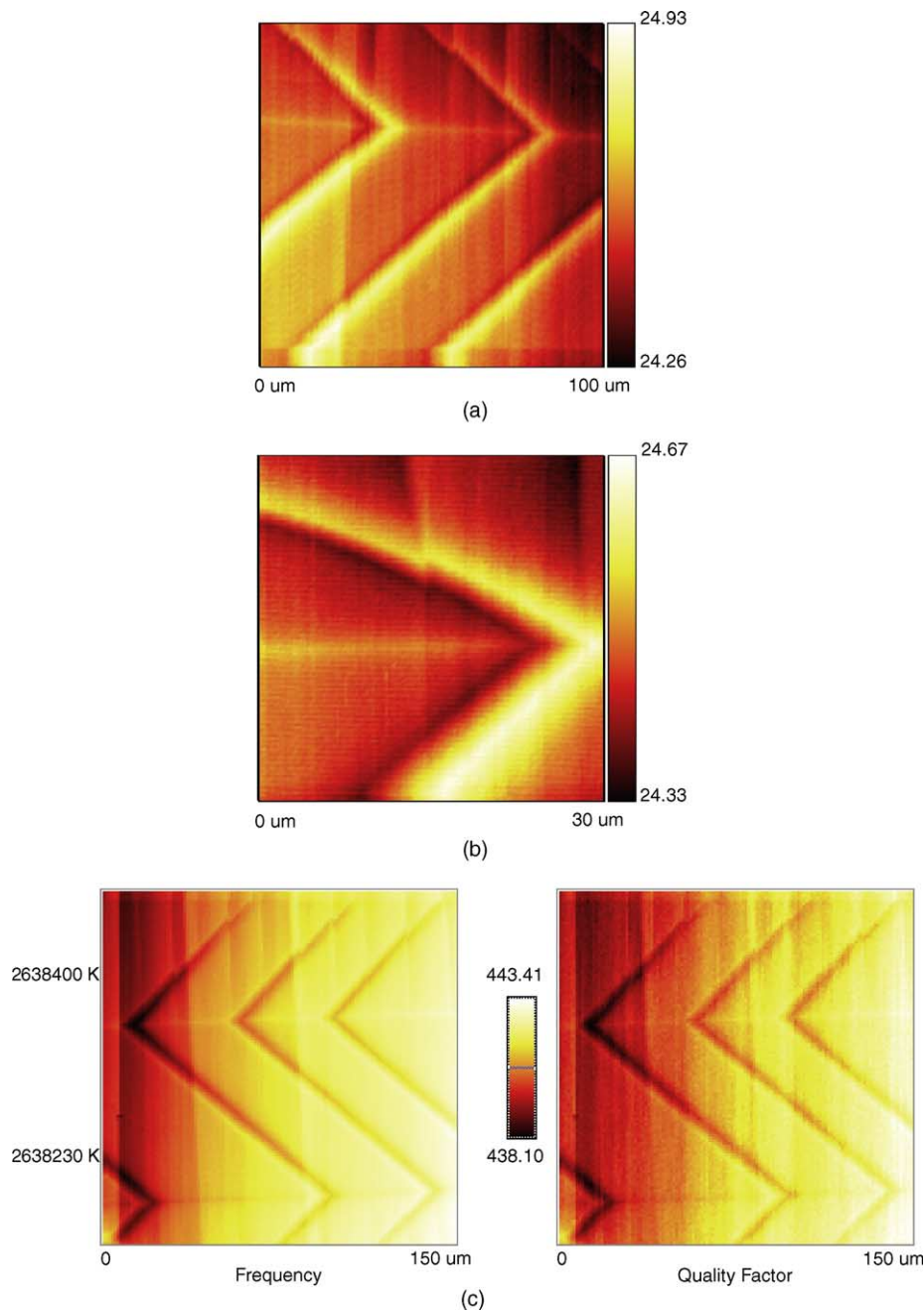

Fig. 6. SMM images of twin structures in a LaAlO$_3$ crystal: (a) lower magnification dielectric constant image taken by motor-scan; (b) higher magnification dielectric constant image taken by piezo scan; (c) Resonant frequency and quality factor images of twin structures.

horizontal lines in Fig. 6. Moreover, the dielectric constant of the more numerous ⟨1 0 0⟩ twins is lower than that of the ⟨1 1 0⟩ twins. The angle between the intersecting twins shown in the higher magnification image in Fig. 6b should be 90°. The non-perpendicular intersection is an artifact of the *xy*-piezotube scanning, which is not seen in the coarser, motor-scanned images, such as Fig. 6a and c.

The greater contrast associated with the ⟨1 0 0⟩ twins relative to the ⟨1 1 0⟩ twins is likely due to strain differences between the two twin types. In $Ba_xSr_{1-x}TiO_3$ thin films, for example, it has been shown that the dielectric constant is very sensitive to strain levels. In the work of Kim et al.[15] the dielectric constant exhibits a maximum as a function of strain. For LAO, it has not been determined what the relationship between dielectric constant and strain is in the crystals. Thus, based on the image alone we cannot say which twin exhibits higher strain. However, reports indicate that (1 0 0) twins have smaller total strain than (1 1 0) twins (∼87% of the 1 1 0 value).[11]

3.2. Interface of oxygen-rich and oxygen-poor titania crystals

Oxygen stoichiometry variations in oxide ceramics can affect dielectric properties, and, thus, can be studied in the SMM. Oxygen-deficient titania is a semiconductor and, therefore, has a higher dielectric loss than stoichiometric TiO_2. When an oxygen-deficient titania single crystal is annealed at high oxygen partial pressure, if the oxygen diffuses only partially into the crystal, it will result in an oxygen-deficient core surrounded by stoichiometric titania. Conversely, a stoichiometric core will be produced when a stoichiometric single crystal is annealed for short period at low partial oxygen pressure. Coring of TiO_2 has been extensively studied (e.g. Templeton et al.[16] and references, therein). Stoichiometric TiO_2 is transparent while oxygen-deficient material has a characteristic blue–gray appearance. In the present study an optical traveling solvent float zone (TSFZ) system[17] (Crystal System Inc., model: FZ-T-10000-H-VI-PV) was used to grow a titania crystal
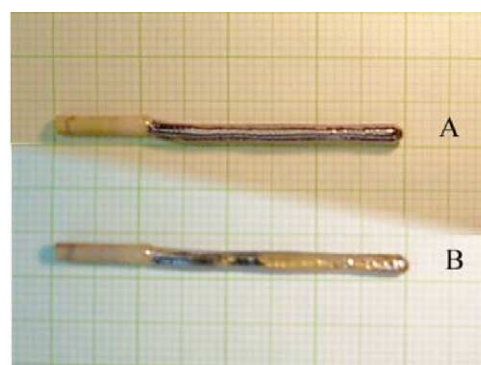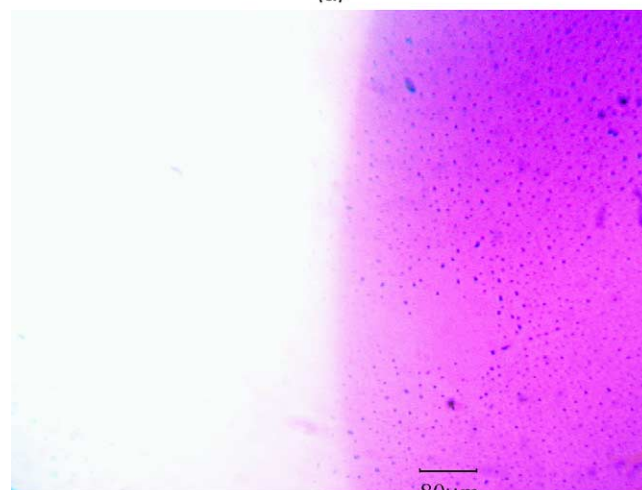
Fig. 7. (a) As-grown titania crystal (A) and annealed crystal (B). (b) Polarized optical microscope image of the cross-section of the crystal (B), showing the interface boundary between the cored and uncored regions of the titania. The lighter region is oxygen-rich.

in air, which results in a non-stoichiometric bluish crystal. This crystal was then annealed in flowing O_2 at 400 °C for 6 h to produce a partially oxygenated "cored" crystal. The crystal before (A) and after (B) annealing is shown in Fig. 7a. The crystal was subsequently sliced and polished,
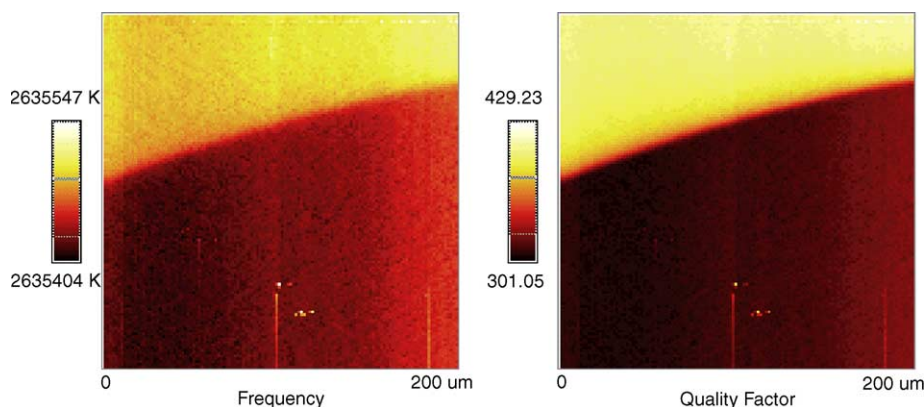

Fig. 8. Resonant frequency (left) and Q (right) SMM images near the interface boundary of the titania. The darker region is oxygen depleted.
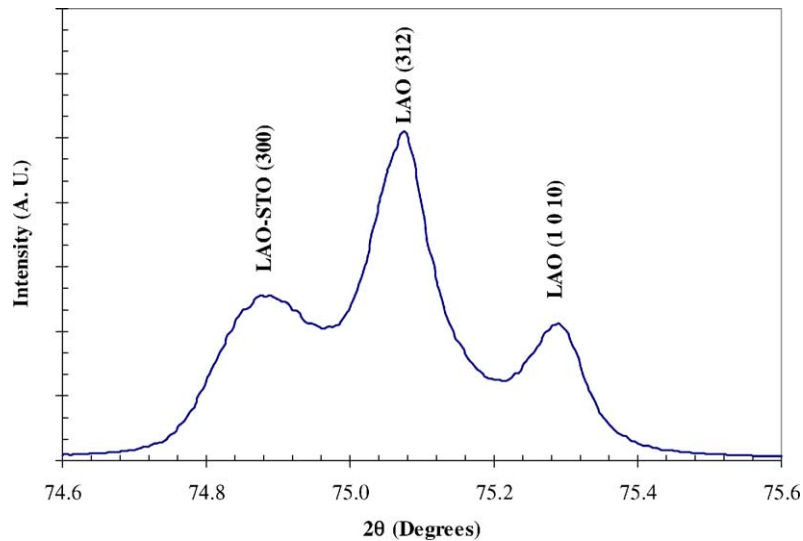
Fig. 9. Diffraction pattern of the LAO side of the LaAlO₃–SrTiO₃ interface; a solid solution (3 0 0) peak along with LAO rhombohedral (3 1 2) and (1 0 1 0) peaks are seen.

yielding a sample with a well-defined boundary between the stoichiometric and non-stoichiometric regions. Fig. 7b shows a polarized optical microscope image of the boundary region. The purple (dark) region is the oxygen-deficient material. In the oxygen-deficient region, some Ti^{4+} is reduced to Ti^{3+} and oxygen vacancies are formed. This is thought to be responsible for drastic reductions in the quality factor. These vacancies may subsequently aggregate to form pores during annealing. Thus, more pores are observed in the oxygen-deficient region than in the oxygen-rich region. Fig. 8 is a SMM image near the interface scanned in soft-contact mode with large scale scanning. As expected, the dielectric loss of the blue (oxygen-deficient) region was higher than that of the better oxygenated region. The difference of quality factor between these two regions was about 100. In this case the contrast of the SMM image is introduced by the effect of chemical variation (oxygen concentration) on dielectric properties.

3.3. Interface of diffusion couple of LAO–STO

In the case of TiO_2 above, oxygen non-stoichiometry led to a change in dielectric constant, and, thus, to a contrast in the SMM. There the difference in quality factor was large and the interface region was relatively short. Dielectric property changes across an interphase boundary can also be imaged. The dielectric properties near the interface of a diffusion couple of LaAlO₃–SrTiO₃ were studied. Commercially available LaAlO₃ (1 0 0) and SrTiO₃ (1 0 0) single crystals (5 mm × 5 mm × 0.5 mm) were used. The crystals were stacked face to face and sandwiched between two larger LaAlO₃ polycrystalline sintered compacts. The assembly was placed in a furnace and annealed in air at 1450 °C for 24 h. Although unintended, upon removal from the furnace the diffusion couple fractured. The resulting in-
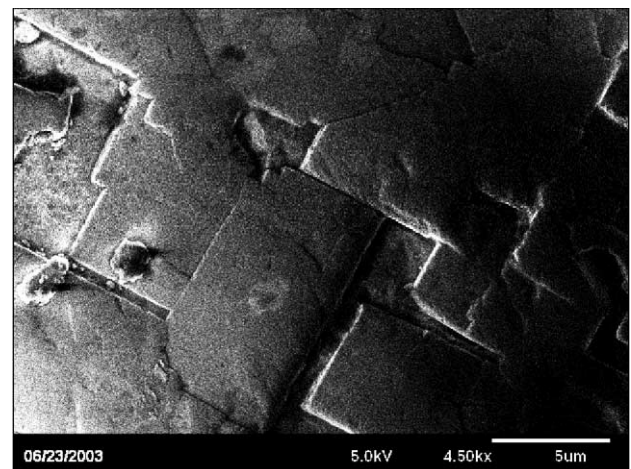
(a)
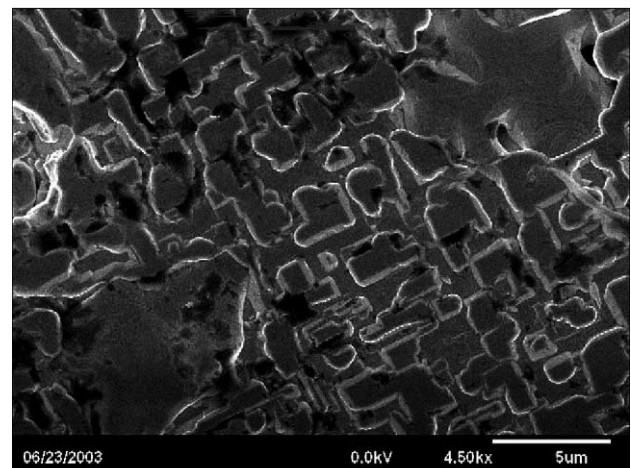
(b)

Fig. 10. SEM images of the (a) LAO side and (b) STO side of the LaAlO₃–SrTiO₃ interface.

terface between the two crystals was relatively weak while the single crystals were strongly bonded with the LaAlO$_3$ compacts. The hoped-for investigation of the cross-section of diffusion couple did not occur, but the fractured interface provided a chance to investigate the fracture surfaces.

Examination indicated that some inter-diffusion did occur. Powder X-ray diffraction was used to examine the LAO side of the interface to look for evidence of inter-diffusion. LAO and STO have solid solubility in the entire composition range.[18] The time and temperature used to anneal the LAO–STO diffusion couple caused a very thin layer of a solid solution on the top of the LAO single crystal. As shown in Fig. 9, lines characteristic of LAO as well as a LAO–STO solid solution are observed on the LAO fracture surface. The peak of the solid solution of LAO and STO appears in the XRD pattern at $2\theta = 74.9°$, along with two peaks resulting from splitting of the LAO pseudo cubic (3 0 0) peak into (3 1 2) and (1 0 1 0) rhombohedral peaks. The (3 0 0) LAO–STO line is displaced to a 2θ angle lower than that in the LAO alone, due to the atomic radii differences between Sr and Ti relative to La and Al. The (3 0 0) STO line is at $2\theta = 72.54°$. The solid solution peak is very close to pseudo (3 0 0) LAO line, indicating that the solid solution is LAO-rich.

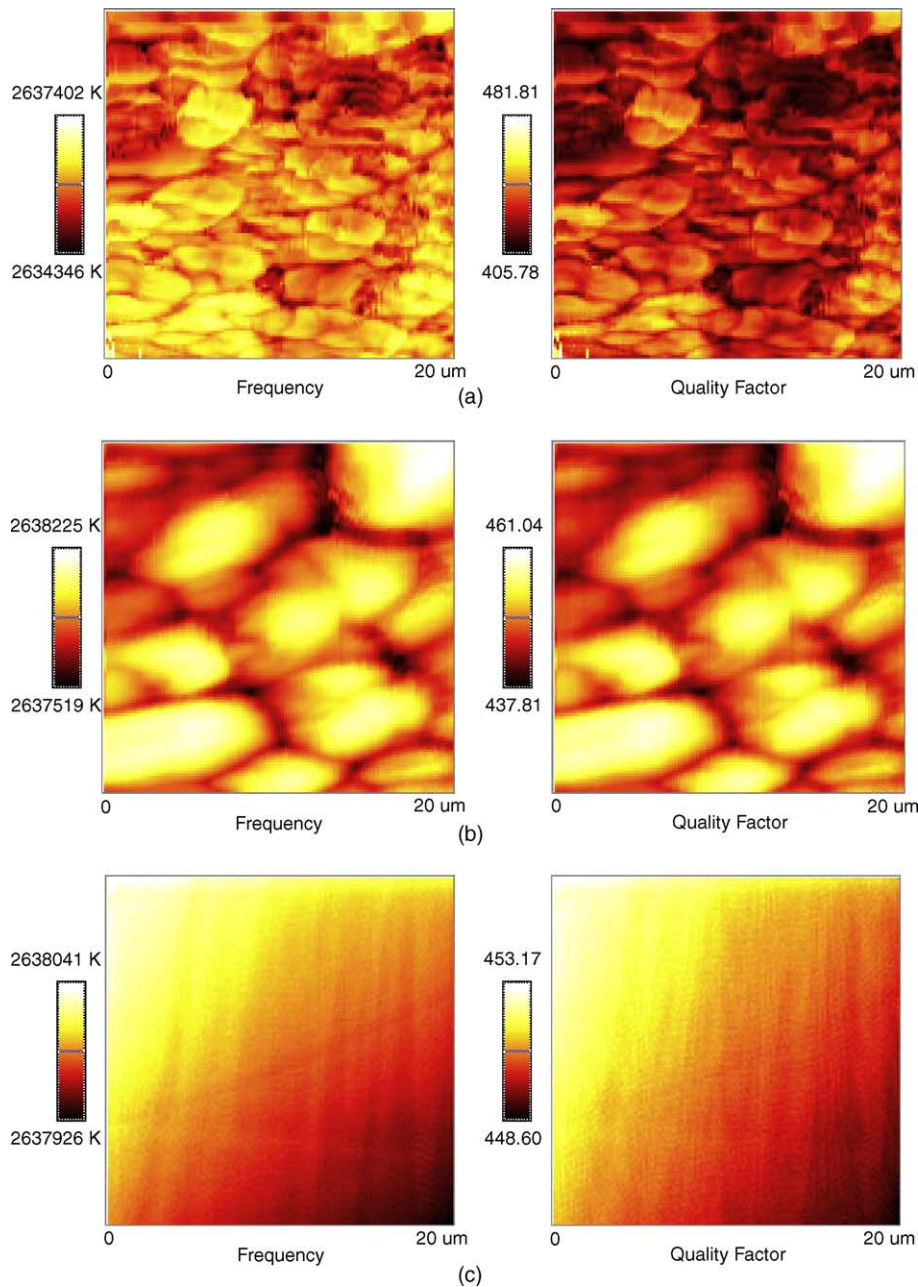Fig. 11. Resonant frequency (left) and Q (right) SMM images of: (a) the STO side of the LaAlO$_3$–SrTiO$_3$ interface; (b) the LAO side of the LaAlO$_3$–SrTiO$_3$ interface; (c) the unreacted LAO crystal (without STO diffusion).

An attempt was made to examine each of the fracture surfaces with the SMM as well as by scanning electron microscopy (SEM). SEM inspection (Fig. 10) shows growing platelets at the interface. In addition, some *Z* (atomic number) contrast was caused by the backscatter electrons (Fig. 10a), presumably due to inter-diffusion between the crystals.

Since the fracture surface roughness was large, it was difficult to perform a large soft-contact scan on the interface surface. Only the dielectric properties within small regions could be examined. Fig. 11a shows the rough surface on the STO side of the interface, while Fig. 11b shows an SMM image on the LAO side of the interface. The roughness of the interfaces introduces a large amount of contrast, which is evident in comparison with Fig. 11c, which shows a region on the LaAlO$_3$ crystal that experienced no STO diffusion (due to crystal misalignment). On the unreacted LAO in Fig. 11c, the resonant frequency is very uniform, with a variation of only 115 kHz, and *Q* varies from 448.6 to 453.17. In contrast, there are large variations of resonant frequency and *Q* on both the STO and LAO sides of the interface. Because the inter-diffusion distance is short, an effect of the underlying base crystal still exists, so the resonant frequencies are close to those of the base crystals. The resonant frequencies of LAO and STO single crystals are 2638.53 and 2633.76 MHz, respectively. The resonant frequency of the LAO side of the fractured interface is lower than that of the LAO single crystal while the STO side is higher than that of the STO single crystal. This indicates, as one might expect, that the resonant frequency of the LAO–STO solid solution will be between the values of the LAO and STO single crystals. Unfortunately, a more quantitative assessment of the solid solution dielectric values cannot be achieved with this interface geometry. Future studies looking at a cross-section of the interface should resolve this issue.

3.4. Grain boundaries of yttria-stabilized zirconia polycrystalline substrate

The SMM images so far have shown contrast resulting from topography, strain and chemical variations. Imaging of the dielectric properties in polycrystalline ceramic samples presents other complexities. A yttria-stabilized zirconia (YSZ) substrate obtained from Intertec Southwest Inc. was examined by both atomic force microscopy (AFM) and SMM. The AFM images were found to aid in the interpretation of the SMM image. An AFM topographic image of the as-received YSZ substrate is shown in Fig. 12. The grain boundaries are readily apparent and the relative roughness of the surface is seen to be greater than 0.2 μm. An example SMM image of the YSZ substrate scanned by soft-contact mode with the sharp tip is shown in Fig. 13a. Because the AFM tip is much smaller than the sharp tip of the SMM (about 10–20 μm), the resolution of AFM is much higher than that of SMM. The contrast in the SMM image results from both topographic effects and dielectric properties variations. The outlines of grains and apparent intergranular defects are observed in the SMM image. The resonant frequency and quality factor at grain boundaries and near the centers of some grains were both lower than that in the bulk of the grains, as evidenced by the darker color of those features in the images.

As seen in the AFM images, the grain boundaries are grooved and the grains surfaces also are not flat. When the SMM tip is near a surface depression (e.g. grain boundary groove), the extent of interaction will be greater than that
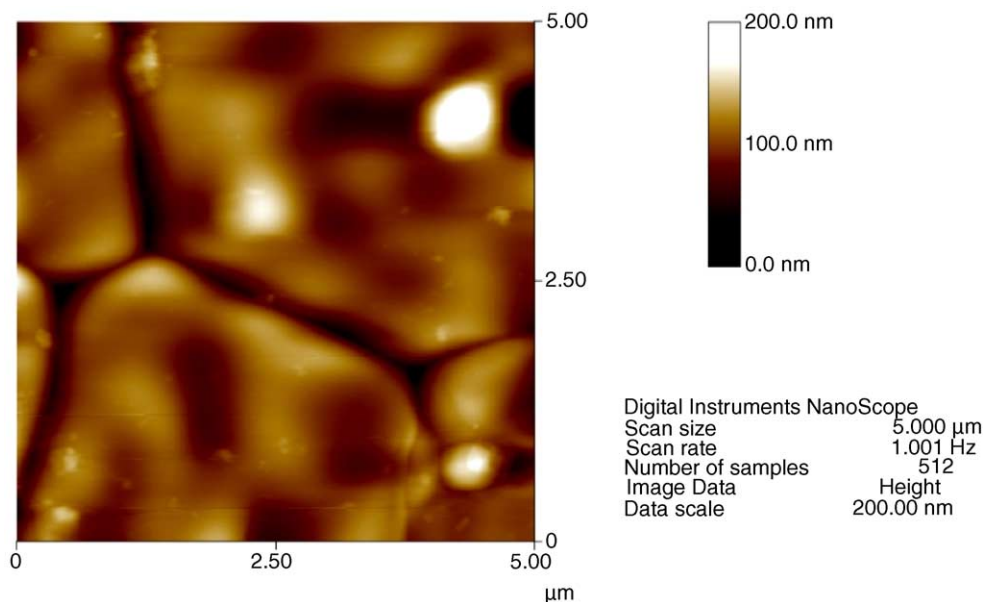

Fig. 12. AFM image of the as-received YSZ substrate, showing the grain boundaries and surface topography.

for a flat surface,[19] resulting in a lower resonant frequency. Therefore, the SMM images represent depressions as being darker in soft-contact mode, i.e. non-planar surfaces result in contrast in SMM images. Hence, it can be difficult to separate the causes for a decrease in resonant frequency, which could be due to chemical segregation or compositional non-uniformity effects, as opposed to the aforementioned topographic effect.

In order to minimize topographic effects, the YSZ substrate was polished and again examined with the SMM. As seen in Fig. 13b, some of the grain boundaries and defects still can be distinguished after polishing, although with less contrast than in Fig. 13a. And Fig. 13c is an SMM image of a well polished region, where the grain boundaries are unable to be clearly distinguished. In these images defects with larger scale than grain boundaries (e.g. pores, inclusions) contribute most of the contrast in dielectric constant image. Here there is insufficient contrast to adequately resolve the grain boundaries.

This illustrates that it can be difficult to separate topography effects from other contrast producing effects (e.g. compositional variations) based on SMM images alone. For
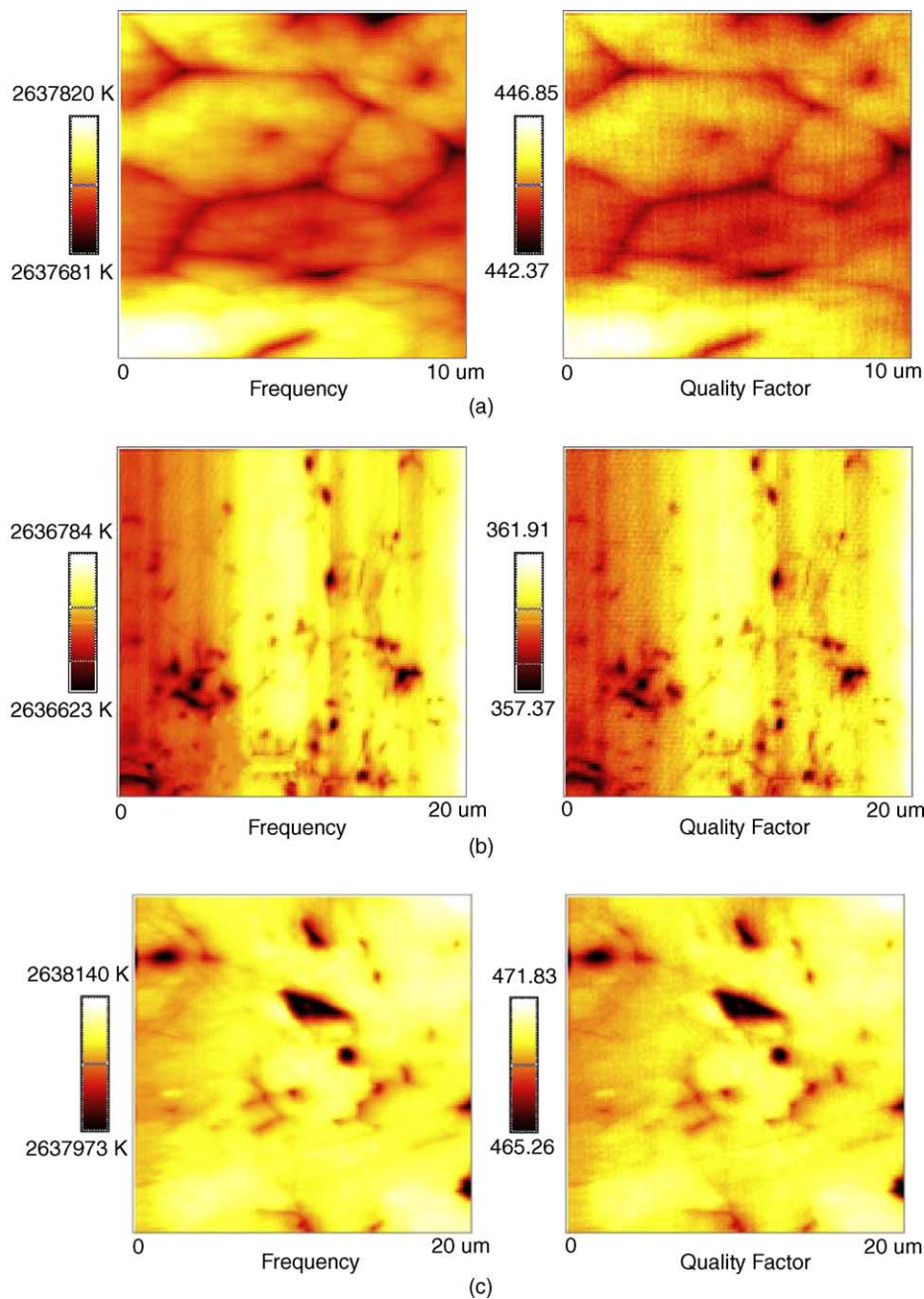

Fig. 13. Resonant frequency (left) and *Q* (right) SMM images of: (a) the as-received YSZ substrate showing grain boundary outlines; (b) the partially polished YSZ substrate with fainter grain boundary contrast; (c) the well polished YSZ substrate, where grain boundaries are now difficult to distinguish.

example, grain boundaries are typically the preferred site for impurity or dopant segregation. This may alter dielectric behavior relative to the grain interior, thus enhancing image contrast. In the YSZ sample, polishing reduced the contrast in Fig. 13a to that seen in Fig. 13c, suggesting that the grain boundaries in this sample do not have significantly different dielectric properties from the grain interiors. This is desirable if uniform properties are the goal, but less helpful for microstructure observations. This emphasizes that SMM observations will be enhanced by being coupled with microprobe or SEM/EDXS characterization to verify the presence or absence of chemical effects.

4. Conclusions

Near-field scanning microwave microscopy permits quantitative characterization and imaging of bulk dielectrics on a local scale. The contrast for image production can be the result of topographic effects as well as dielectric property variations. Topographic effects in bulk samples can be minimized by careful surface preparation. Strain and composition variations can both affect local dielectric behavior and lead to image contrast. Grain boundaries, twin domains, diffusion interface and defects present in the microstructures were observed in the SMM images.

Acknowledgements

References

1. Vanderah, T. A., Talking ceramics. *Science* 2002, **298**(5596), 1182–1184.
2. Xiang, X. D. and Gao, C., Quantitative complex electrical impedance microscopy by scanning evanescent microwave microscope. *Mater. Charact.* 2002, **48**(2/3), 117–125.
3. Rosner, B. T. and van der Weide, D. W., High-frequency near-field microscopy. *Rev. Sci. Instrum.* 2002, **73**(7), 2505–2525.
4. Steinhauer, D. E., Vlahacos, C. P., Wellstood, F. C., Anlage, S. M., Canedy, C., Ramesh, R. *et al.*, Imaging of microwave permittivity, tunability, and damage recovery in (Ba,Sr)TiO$_3$ thin films. *Appl. Phys. Lett.* 1999, **75**(20), 3180–3182.
5. Wang, Y. G., Reeves, M. E. and Rachford, F. J., Simultaneous imaging of dielectric properties and topography in a PbTiO$_3$ crystal by near-field scanning microwave microscopy. *Appl. Phys. Lett.* 2000, **76**(22), 3295–3297.
6. Chang, H., Takeuchi, I. and Xiang, X. D., A low-loss composition region identified from a thin-film composition spread of (Ba$_{1-x-y}$Sr$_x$Ca$_y$)TiO$_3$. *Appl. Phys. Lett.* 1999, **74**(8), 1165–1167.
7. Hyun, S., Kim, A., Kwon, J. and Char, K., Dielectric morphology of twin domains in LaAlO$_3$ observed by a scanning microwave microscope. *Jpn. J. Appl. Phys. 1* 2001, **40**(11), 6510–6513.
8. Klein, M. and Schwitzgebel, G., An improved lamellae drop-off technique for sharp tip preparation in scanning tunneling microscopy. *Rev. Sci. Instrum.* 1997, **68**(8), 3099–3103.
9. Gao, C. and Xiang, X. D., Quantitative microwave near-field microscopy of dielectric properties. *Rev. Sci. Instrum.* 1998, **69**(11), 3846–3851.
10. Kim, C. H., Cho, S. Y., Kim, I. T., Cho, W. J. and Hong, K. S., Twin structures in lanthanum, praseodymium, and neodymium aluminate ceramics. *Mater. Res. Bull.* 2001, **36**(9), 1561–1571.
11. Kim, C. H., Jang, J. W., Cho, S. Y., Kim, I. T. and Hong, K. S., Ferroelastic twins in LaAlO$_3$ polycrystals. *Physica B* 1999, **262**(3/4), 438–443.
12. Vanderah, T. A., Lowe-Ma, C. K. and Gagnon, D. R., Synthesis and dielectric properties of substituted lanthanum aluminate. *J. Am. Ceram. Soc.* 1994, **77**(12), 3125–3130.
13. Yao, G. D., Hou, S. Y., Dudley, M. and Phillips, J. M., Synchrotron X-ray topography studies of twin structures in lanthanum aluminate single-crystals. *J. Mater. Res.* 1992, **7**(7), 1847–1855.
14. Sum, R., Lang, H. P. and Guntherodt, H. J., Scanning force microscopy study of single-crystal substrates used for thin-film growth of high-temperature superconductors. *Physica C* 1995, **242**(1/2), 174–182.
15. Kim, L., Jung, D. G., Kim, J., Kim, Y. S. and Lee, J., Strain manipulation in BaTiO$_3$/SrTiO$_3$ artificial lattice toward high dielectric constant and its non-linearity. *Appl. Phys. Lett.* 2003, **82**(13), 2118–2120.
16. Templeton, A., Wang, X. R., Penn, S. J., Webb, S. J., Cohen, L. F. and Alford, N. M., Microwave dielectric loss of titanium oxide. *J. Am. Ceram. Soc.* 2000, **83**(1), 95–100.
17. See http://www.crystalsys.co.jp/products/fzp2.htm for further information about TSFZ.
18. Vess, C. J., Gilmore, J., Kohrt, N. and McGinn, P. J., Combinatorial synthesis of oxide powders with an autopipetting system. *J. Comb. Chem.* 2004, **6**, 86–90.
19. Imtiaz, A. and Anlage, S. M., A novel STM-assisted microwave microscope with capacitance and loss imaging capability. *Ultramicroscopy* 2003, **94**(3/4), 209–216.